Supplementary Report: Cooperative Control of Autonomous Surface Vehicles for Oil Skimming and Cleanup

Subhrajit Bhattacharya, Hordur Heidarsson, Gaurav S. Sukhatme and Vijay Kumar

Abstract

Oil skimmers towed by two vehicles have been widely used for skimming of oil on the water surface. In this paper, we model the skimmer as a flexible, floating rope of constant length as well as discrete segmented model. We derive the equations governing the rope dynamics from first principles and demonstrate their application through simulations. We have performed field experiments with two autonomous surface vehicles that substantiate the proposed model. The experimental analysis provided information about certain parameters in the model. We propose a method for controlling the shape of the rope, and derive the conditions that maximize skimming efficiency.

I. INTRODUCTION

On April 20, 2010 the Deepwater Horizon drilling rig explosion in the Gulf of Mexico caused the largest oil spill (Figure 1) in the history of the petroleum industry. By the time the gushing wellhead was capped (July 15, 2010), it is estimated that approximately $10^4\ m^3$ of crude oil was released into the ocean [9]. Before the wellhead could finally be capped four primary means of mitigation were employed: direct recovery from the wellhead, burning at the surface, chemical dispersion, and skimming at the surface.

Skimming operations at the surface accounted for the smallest impact (by some estimates $\sim 3\%$ of the oil was skimmed [7]). This is not surprising, since skimming (whether with a floating boom deployed from one ship, or via the manipulation of a flexible skimmer using two ships (Figure 1)) is a slow, manual operation. Given, the widespread concern at the use of certain chemicals for dispersion, increased efficiency in skimming operations could lead to positive change in the way cleanup is performed in the future.

Motivated by this, we develop a model of roboticized skimming operations using two Autonomous Surface Vehicles (ASVs) cooperatively towing a flexible skimmer. The model allows us to design controllers for the ASVs and to think about problems beyond skimming, such as caging and towing rigid objects (barges, floating docks *etc.*) using ASVs.

For purposes of the skimming analysis in this paper we will model the skimmer as a flexible, floating rope of constant length. Such a rope has infinite degrees of freedom. When attached at each end to a ASV, it deforms continuously in the horizontal plane under the effects of the forces the vehicles impart at its endpoints and the drag due to the water. The separation between the vehicles, and their instantaneous accelerations govern the deformation of the rope. To the roboticist, several problems present themselves. What is the current shape of the rope (a state estimation problem)? Given a caging or coverage task (*e.g.,* cage a rigid object or cage a deformable object like an oil slick) how does one control the rope so it assumes the appropriate/optimal shape (a 'grasp' planning/optimization problem)? Given a transport task (*e.g.,* tow an object from location A to B) how does one plan and control the sequence of rope shapes so the task is completed (a manipulation problem).

In this paper we model the problem from first principles in the form of PDEs describing the dynamics of the rope (Section II). These equations simplify to the catenary solution at steady state and certain assumptions on the drag coefficients. We then develop a complete dynamic model and simulation with force and position control at the ends of the rope, with the rope approximated by discrete rigid segments (Section III), as well as a quasi-static approximation of it (Section IV). Following this we report on experimental results in field trials to identify the discrete model under quasi-static conditions (inertial forces negligible compared to drag) (Section V) Using the parameters so identified we apply the model to two tasks.

Subhrajit Bhattacharya and Vijay Kumar are with the GRASP Laboratory, University of Pennsylvania. Hordur Heidarsson and Gaurav S. Sukhatme are with the Robotic Embedded Systems Laboratory at the University of Southern California. {subhrabh,kumar}@seas.upenn.edu, {heidarss,gaurav}@usc.edu

Fig. 1. (left) The oil slick caused by the Deep Water Horizon explosion as seen from space by NASA's Terra satellite on May 24, 2010 and (right) a skimming operation with two vessels in the gulf of Mexico.

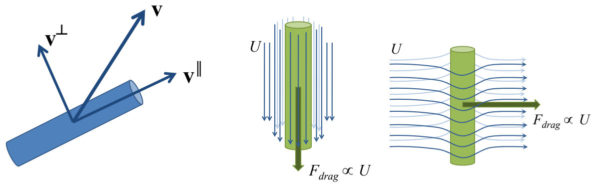

(a) (b) (c)

Fig. 2. Drag on a cylinder due to its motion through a fluid can be split into two components.

The first task is to control the rope shape so that it is transformed from its initial configuration into a (desired) steady state (Section VI). The second is to sweep an area given a maximum force that the boats can exert (*i.e.,* maximum drag force) and a fixed rope length. We solve for the maximum speed for a given boat-to-boat desired separation under these constraints. We also solve for the maximum efficiency (swept area per unit time) we can achieve for cleanup in such a setting (Section VI). The paper concludes (Section VII) with a discussion summarizing the results and identifying problems for future work.

II. Continuous Dynamic Model

We begin by deriving the dynamic model of the continuous flexible rope.

A. Drag Force Model

We consider the drag force on a small cylindrical element moving in a fluid with a velocity $\mathbf{v}$ at low Reynolds number. We assume that the diameter of the cylinder is much smaller than the length. The velocity of the element can be decomposed into two components - one parallel to the axis ($\mathbf{v}^{\parallel}$), other perpendicular to the axis ($\mathbf{v}^{\perp}$). At low Reynolds number the drag forces are assumed to be proportional (linear) to the speed, but the proportionality constants are different along the parallel and perpendicular directions. In particular, we write the drag force per unit length, $\mathbf{f}_D$, acting on the cylindrical element (Figure 2(a)) that is moving through a fluid with velocity $\mathbf{v}$ as follows:

$$\mathbf{f}_D = -\left(c_V \mathbf{v}^{\parallel} + c_S \mathbf{v}^{\perp}\right) \tag{1}$$

where c_S and c_V are constants that are functions of the standard properties of the fluid such as Reynolds number (Re), drag coeficient (C_D), dynamic viscosity (μ) and density (ρ).

For flow perpendicular to the axis of a cylinder of diameter d, at low Reynold's number ($Re \leq 100$), the drag coeficient, C_D, varies inversely as Re, and is 1 at $Re = 100$ [10], [4]. Noting that f_S (force per unit length on the cylinder due to flow perpendicular to axis) $= \frac{1}{2} C_D \rho d U^2$ we can thus empirically derive a value for c_S as follows,

$$\begin{aligned} c_S &= \frac{f_S}{U}(\text{by definition}) = \frac{1}{2} C_D \ \rho \ d \ U = \frac{1}{2}\frac{100}{Re} \ \rho \ d \ U \\ &= \frac{100}{2}\frac{\mu}{\rho \ d \ U} \ \rho \ d \ U = 50 \ \mu \end{aligned} \tag{2}$$

where μ, the dynamic viscocity, takes the value of 8.9×10^{-4} for fresh water at $25°C$, and 1.08×10^{-3} for sea water at $20°C$. In all simulations we assumed $\mu = 1 \times 10^{-3}$, giving $c_S = 0.05$.

B. The Rope Dynamics

We use s, the length of the rope starting from the *left* boat up to a point $\mathbf{p}$ on the rope, for parametrization of the points on the rope. Thus, we denote the coordinate of a point on the rope in a global reference frame by $\mathbf{p}(s,t) = \begin{bmatrix} x(s,t) \\ y(s,t) \end{bmatrix}$. λ is the mass per unit length of the rope (assumed to be constant). By choice of the parameter s we have the following identity,

$$\left(\frac{\partial x}{\partial s}\right)^2 + \left(\frac{\partial y}{\partial s}\right)^2 = 1 \tag{3}$$

Figure 3(b) shows the free body diagram of an infinitesimal element at a point $\mathbf{p}(s,t)$ on the rope. A simple moment analysis of the element implies that the tension force, $\mathbf{T}$, acts along the direction of the tangent at $\mathbf{p}$. From Newton's Second Law, the dynamics of the element of mass $\lambda \Delta s$ is given by,

$$\lambda \Delta s \ \frac{\partial^2 \mathbf{p}}{\partial t^2} = \begin{bmatrix} T_x(s,t) \\ T_y(s,t) \end{bmatrix} - \left(c_V \mathbf{v}^{\parallel} + c_S \mathbf{v}^{\perp}\right) \Delta s \tag{4}$$

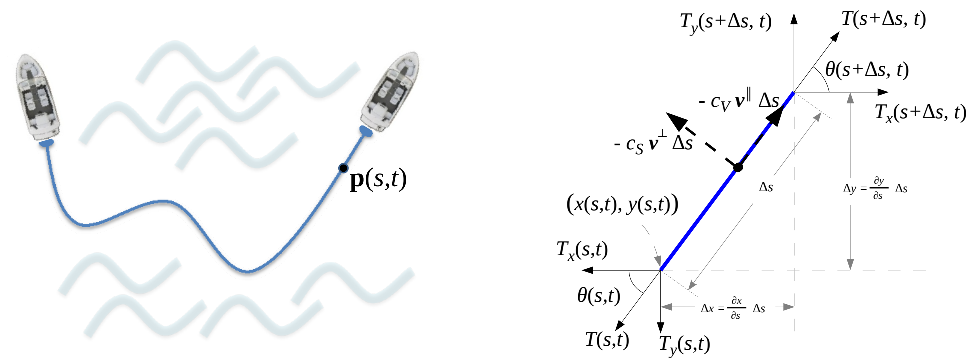

(a) Two boats towing a rope.

(b) Free body diagram of an infinitesimal rope element at $\mathbf{p}$.

Fig. 3. The continuous planar deformation model for the rope.

However, we note that from the moment equation, $\mathbf{T} = \begin{bmatrix} T_x(s,t) \\ T_y(s,t) \end{bmatrix}$ points in the same direction as the tangent vector $\hat{\mathbf{u}}^{\parallel} = \begin{bmatrix} \frac{\partial x}{\partial s} \\ \frac{\partial y}{\partial s} \end{bmatrix}$. The later is a unit vector since the parameter s represents the length along the rope. Thus,

$$\begin{bmatrix} T_x(s,t) \\ T_y(s,t) \end{bmatrix} = T(s,t) \begin{bmatrix} \frac{\partial x}{\partial s} \\ \frac{\partial y}{\partial s} \end{bmatrix} = T(s,t) \frac{\partial \mathbf{p}}{\partial s} \tag{5}$$

where T is the magnitude of the tension $\mathbf{T}$. Thus, taking $\Delta s \to 0$, equation (4) reduces to,

$$\lambda \frac{\partial^2 \mathbf{p}}{\partial t^2} = \frac{\partial}{\partial s}\left(T \frac{\partial \mathbf{p}}{\partial s}\right) - c_V \mathbf{v}^{\parallel} - c_S \mathbf{v}^{\perp} \tag{6}$$

Again, the resolution of the velocity vector, $\mathbf{v} = \begin{bmatrix} \frac{\partial x}{\partial t} \\ \frac{\partial y}{\partial t} \end{bmatrix}$ along the tangent, $\hat{\mathbf{u}}^{\parallel} = \begin{bmatrix} \frac{\partial x}{\partial s} \\ \frac{\partial y}{\partial s} \end{bmatrix}$, and perpendicular to the tangent, $\hat{\mathbf{u}}^{\perp} = \begin{bmatrix} -\frac{\partial y}{\partial s} \\ \frac{\partial x}{\partial s} \end{bmatrix}$, gives,

$$\begin{aligned} \mathbf{v}^{\parallel} &= (\mathbf{v} \cdot \hat{\mathbf{u}}^{\parallel})\hat{\mathbf{u}}^{\parallel} = \begin{bmatrix} \left(\frac{\partial x}{\partial t}\frac{\partial x}{\partial s} + \frac{\partial y}{\partial t}\frac{\partial y}{\partial s}\right)\frac{\partial x}{\partial s} \\ \left(\frac{\partial x}{\partial t}\frac{\partial x}{\partial s} + \frac{\partial y}{\partial t}\frac{\partial y}{\partial s}\right)\frac{\partial y}{\partial s} \end{bmatrix} \\ \mathbf{v}^{\perp} &= (\mathbf{v} \cdot \hat{\mathbf{u}}^{\perp})\hat{\mathbf{u}}^{\perp} = \begin{bmatrix} \left(-\frac{\partial x}{\partial t}\frac{\partial y}{\partial s} + \frac{\partial y}{\partial t}\frac{\partial x}{\partial s}\right)\left(-\frac{\partial y}{\partial s}\right) \\ \left(-\frac{\partial x}{\partial t}\frac{\partial y}{\partial s} + \frac{\partial y}{\partial t}\frac{\partial x}{\partial s}\right)\frac{\partial x}{\partial s} \end{bmatrix} \end{aligned} \tag{7}$$

Substituting (7) into (6), along with the property (3) of the parametrization s, we obtain the complete set of partial differential equations (PDEs) governing the dynamics of the rope as follows,

$$\begin{aligned} &\lambda \frac{\partial^2 x}{\partial t^2} = \frac{\partial}{\partial s}\left(T\frac{\partial x}{\partial s}\right) - c_V\left(\frac{\partial x}{\partial t}\frac{\partial x}{\partial s} + \frac{\partial y}{\partial t}\frac{\partial y}{\partial s}\right)\frac{\partial x}{\partial s} \\ &\qquad\qquad - c_S\left(-\frac{\partial x}{\partial t}\frac{\partial y}{\partial s} + \frac{\partial y}{\partial t}\frac{\partial x}{\partial s}\right)\left(-\frac{\partial y}{\partial s}\right) \\ &\lambda \frac{\partial^2 y}{\partial t^2} = \frac{\partial}{\partial s}\left(T\frac{\partial y}{\partial s}\right) - c_V\left(\frac{\partial x}{\partial t}\frac{\partial x}{\partial s} + \frac{\partial y}{\partial t}\frac{\partial y}{\partial s}\right)\frac{\partial y}{\partial s} \\ &\qquad\qquad - c_S\left(-\frac{\partial x}{\partial t}\frac{\partial y}{\partial s} + \frac{\partial y}{\partial t}\frac{\partial x}{\partial s}\right)\frac{\partial x}{\partial s} \\ &\left(\frac{\partial x}{\partial s}\right)^2 + \left(\frac{\partial y}{\partial s}\right)^2 = 1 \end{aligned} \tag{8}$$

The three equations in (8) contain three unknown quantities, x, y and T. Given appropriate initial and boundary conditions these can be solved numerically. Typically it is difficult to find an analytic solution to such equations (*Nonlinear Wave Equations*). In this paper we do not attempt to solve these PDEs directly. In Section III we propose a discrete model for the problem and numerically obtain solutions for the discrete model instead. The discrete model is a reduced order approximation of the exact continuous model described in this section.

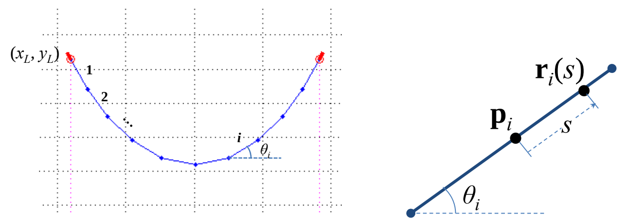

(a) A discrete dynamic model consisting of n rigid segments.

(b) The i^{th} segment.

Fig. 4. A discrete dynamic model.

C. A Special Case - The Catenary Analogy

We consider the special case of steady-state motion of the system along a straight line by making both boats drive at constant parallel velocities. Without loss of generality we can assume that the motion is along the positive Y axis with speed v. Thus we have $\frac{\partial x}{\partial t} = 0$, $\frac{\partial y}{\partial t} = v$

For this case, a quick simplification of equations (8) can be made using the following two assumptions:

i. The inertial foces are negligible compared to the viscous forces, *i.e.* quasi-static motion.
ii. $c_V = c_S = c$, *i.e.* the drag coefficients along the parallel and perpendicular directions are equal.

In the later sections of this paper we will emphasis the fact that the aforesaid assumptions indeed hold in many practical cases, and substantiated by experiments.

Under these assumptions the set of equations (8) reduces to the following ordinary differential equations (ODEs) describing the shape of the rope.

$$\begin{aligned} \frac{\mathrm{d}}{\mathrm{d}s}\left(T\frac{\mathrm{d}x}{\mathrm{d}s}\right) &= 0 \\ \frac{\mathrm{d}}{\mathrm{d}s}\left(T\frac{\mathrm{d}y}{\mathrm{d}s}\right) &= cv \\ \left(\frac{\mathrm{d}x}{\mathrm{d}s}\right)^2 + \left(\frac{\mathrm{d}y}{\mathrm{d}s}\right)^2 &= 1 \end{aligned} \tag{9}$$

This well-known set of ODEs describes the shape of a *Catenary* [2]. Upon integration and elimination of T and s one obtains $y = \frac{T_x}{cv}\cosh\left(\frac{cv}{T_x}x + k_1\right) + k_2$, where the integration constant T_x is the X-component of the force applied by each vehicle, and the integration constants k_1 and k_2 are determined by the choice of coordinate systems. If we choose a coordinate system moving concurrently with the steady-state rope and with origin at the lowest point of the rope, we obtain $y = \frac{T_x}{cv}\cosh\left(\frac{cv}{T_x}x\right) - 1$ (Figure 7(a)). In prior work [1], we have exploited this analogy and designed controllers for the capture and transport of floating targets using a rope and two ASVs.

III. A DISCRETE DYNAMIC MODEL AND SIMULATION

As noted earlier, the accurate solution to Equations (8) is rather difficult to achieve. Thus we propose an approximate discrete model, where the rope is represented by n rigid cylindical segments connected to each other by revolute joints (Figure 4).

A. Force Controlled System

In this section we assume that the external input quantities are the forces applied by the *left* and *right* boats, respectively denoted by $\begin{bmatrix} f_{Lx} \\ f_{Ly} \end{bmatrix}$ and $\begin{bmatrix} f_{Rx} \\ f_{Ry} \end{bmatrix}$. This requires each boat to control the forces applied to the cables. The system has $n+2$ degrees of freedom, and we choose the generalized coordinates to be the coordinates of the point at which the rope is attached to the *left* boat, (x_L, y_L), and the angles made by each of the n segments with the positive X axis, $\theta_i, i = 1, \cdots, n$, all with respect to a global inertial frame of reference.

The position of the center of mass of the i^{th} segment is given by,

$$\mathbf{p}_i = \begin{bmatrix} x_L \\ y_L \end{bmatrix} + \sum_{j=1}^{i-1} L_j \begin{bmatrix} \cos(\theta_j) \\ \sin(\theta_j) \end{bmatrix} + \frac{L_i}{2}\begin{bmatrix} \cos(\theta_i) \\ \sin(\theta_i) \end{bmatrix} \tag{10}$$

where L_j is the length of the j^{th} segment. Thus the velocity of a point, $\mathbf{r}_i(s)$, at a distance s from its center (Figure 4(b)) is given by,

$$\begin{aligned}\dot{\mathbf{r}}_i(s) &= \frac{\mathrm{d}}{\mathrm{d}t}\left(\mathbf{p}_i + s\begin{bmatrix}\cos(\theta_i)\\ \sin(\theta_i)\end{bmatrix}\right) \\ &= \begin{bmatrix}\dot{x_L}\\ \dot{y_L}\end{bmatrix} + \sum_{j=1}^{i-1} L_j\dot{\theta_j}\begin{bmatrix}-\sin(\theta_j)\\ \cos(\theta_j)\end{bmatrix} + \left(\frac{L_i}{2}+s\right)\begin{bmatrix}-\sin(\theta_i)\\ \cos(\theta_i)\end{bmatrix}\dot{\theta}_i\end{aligned} \tag{11}$$

We also define the position of the *right* end of the rope in terms of the generalized coordinates as,

$$\begin{bmatrix}x_R\\ y_R\end{bmatrix} = \begin{bmatrix}x_L\\ y_L\end{bmatrix} + \sum_{j=1}^{n} L_j\begin{bmatrix}\cos(\theta_j)\\ \sin(\theta_j)\end{bmatrix} \tag{12}$$

Following the same approach as in Section II-B, we define $\hat{\mathbf{u}}_i^{\|} = \begin{bmatrix}\cos(\theta_i)\\ \sin(\theta_i)\end{bmatrix}$ and $\hat{\mathbf{u}}_i^{\perp} = \begin{bmatrix}-\sin(\theta_i)\\ \cos(\theta_i)\end{bmatrix}$. Thus we define,

$$\begin{aligned}\mathbf{v}_i^{\|}(s) &= \left(\hat{\mathbf{u}}_i^{\|}\cdot\dot{\mathbf{r}}_i(s)\right)\ \hat{\mathbf{u}}_i^{\|} \\ \mathbf{v}_i^{\perp}(s) &= \left(\hat{\mathbf{u}}_i^{\perp}\cdot\dot{\mathbf{r}}_i(s)\right)\ \hat{\mathbf{u}}_i^{\perp}\end{aligned} \tag{13}$$

The net external force and torque due to drag on the i^{th} segment is thus given by,

$$\begin{aligned}\mathbf{F}_i := \begin{bmatrix}F_{i,x}\\ F_{i,y}\end{bmatrix} &= -\int_{-L_i/2}^{L_i/2}\left(c_V\mathbf{v}_i^{\|}(s) + c_S\mathbf{v}_i^{\perp}(s)\right)ds \\ \tau_i &= -\int_{-L_i/2}^{L_i/2}\mathbf{r}_i(s)\times\left(c_V\mathbf{v}_i^{\|}(s) + c_S\mathbf{v}_i^{\perp}(s)\right)ds\end{aligned} \tag{14}$$

where, with a slight abuse of notation we implied $[a,b]^T \times [p,q]^T = aq - bp$.

Thus, we define the $n+2$ generalized forces [5],

$$\begin{aligned}Q_{x_L} &= \begin{bmatrix}f_{Lx}\\ f_{Ly}\end{bmatrix}\cdot\frac{\partial\begin{bmatrix}x_L\\ y_L\end{bmatrix}}{\partial x_L} + \begin{bmatrix}f_{Rx}\\ f_{Ry}\end{bmatrix}\cdot\frac{\partial\begin{bmatrix}x_R\\ y_R\end{bmatrix}}{\partial x_L} + \sum_{j=1}^{n}\mathbf{F}_j\cdot\frac{\partial\mathbf{p}_j}{\partial x_L} \\ &= f_{Lx} + f_{Rx} + \sum_{j=1}^{n}F_{j,x} \\ Q_{y_L} &= f_{Ly} + f_{Ry} + \sum_{j=1}^{n}F_{j,y} \\ Q_{\theta_i} &= -f_{Rx}L_i\sin(\theta_i) + f_{Ry}L_i\cos(\theta_i) + \tau_i + \sum_{j=1}^{n}\mathbf{F}_j\cdot\frac{\partial\mathbf{p}_j}{\partial\theta_i} \\ &\qquad \forall\ i = 1,2,\cdots,n\end{aligned} \tag{15}$$

The Kinetic Energy of the system is given by,

$$K = \sum_{i=1}^{N}\left(\frac{1}{2}m_i|\dot{\mathbf{p}}_i|^2 + \frac{1}{2}\frac{m_iL_i^2}{12}|\dot{\theta}_i|^2\right) \tag{16}$$

The Lagrange equations of motion [5] are given by,

$$\frac{d}{dt}\left(\frac{\partial K}{\partial\dot{q_l}}\right) - \frac{\partial K}{\partial q_l} - Q_{q_l} = 0 \tag{17}$$

$\forall\ \ q_l \in \{x_L, y_L, \theta_1, \theta_2, \cdots, \theta_n\}$

The equations (17) consist of $n+2$ second order ordinary differential equations in the quantities $\{x_L, y_L, \theta_1, \theta_2, \cdots, \theta_n\}$. Moreover they are affine in $\{\ddot{x}_L, \ddot{y}_L, \ddot{\theta}_1, \ddot{\theta}_2, \cdots, \ddot{\theta}_n\}$. Thus for a given initial values of $\{x_L, y_L, \theta_1, \theta_2, \cdots, \theta_n\}$ and $\{\dot{x}_L, \dot{y}_L, \dot{\theta}_1, \dot{\theta}_2, \cdots, \dot{\theta}_n\}$ at $t = 0$, and given the external force profiles, $\{f_{Lx}, f_{Ly}, f_{Rx}, f_{Ry}\}$ as function of t, we can numerically integrate these equations to obtain the complete dynamics of the system.

For simulating the system we used Mathematica for simplifying the Equations (17) to obtain the ODEs and the coefficients of the second derivatives in the equations. The equations were then numerically integrated using C and Matlab. The accompanying video shows some examples of the simulation results. Figures 5(a)-5(d) shows a trace of the force controlled system simulation.

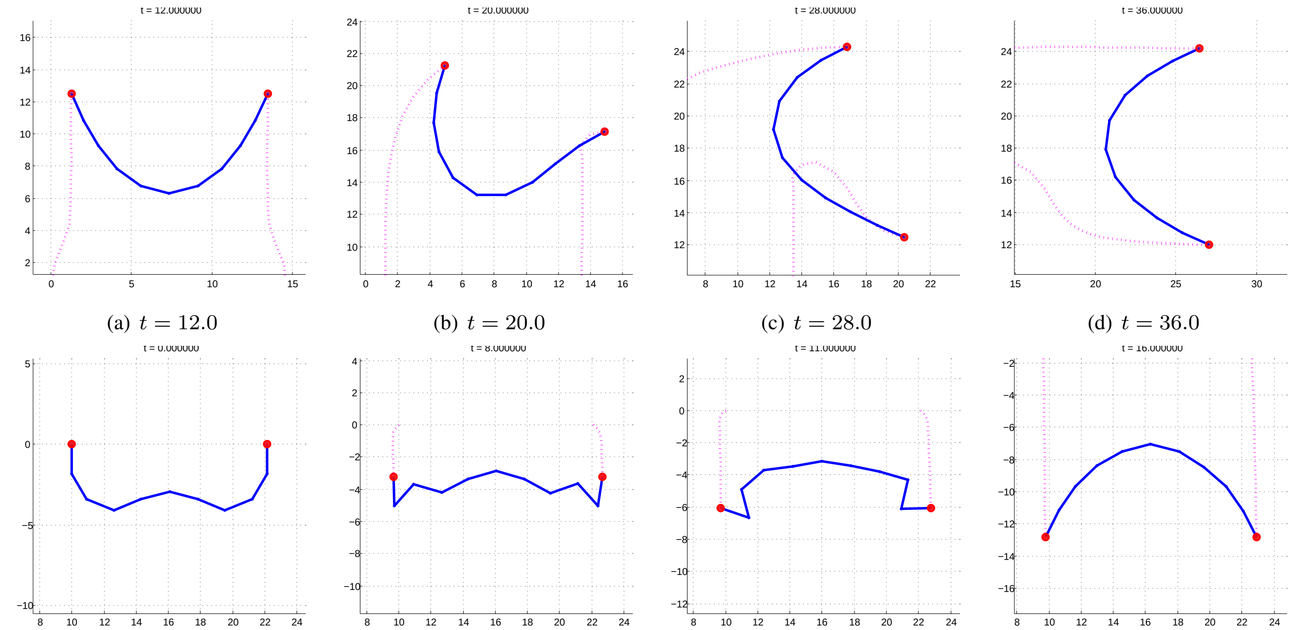

(a) $t = 12.0$ (b) $t = 20.0$ (c) $t = 28.0$ (d) $t = 36.0$

(e) $t = 0.0$ (f) $t = 8.0$ (g) $t = 11.0$ (h) $t = 16.0$

Fig. 5. Traces of complete dynamic simulations of a 10-segment system. Figures 5(a)-5(d) are screenshots from a force-controlled simulation and demonstrates a hard turn to the right. Figures 5(e)-5(h) are screenshots from a position-controlled simulation and demonstrates an "about turn".

B. Position Controlled System

The the force controlled model of the previous section allows us to specify the required values for the forces that the boats need to apply on the rope to achieve a desired trajectory of the end points, in practice it is more realistic to assume that the boats, and therefore the end points, are position controlled. Under such conditions the equations of motion, (17), need to be re-formulated slightly so that now $\{x_L, y_L, x_R, y_R\}$ are the specified variables, and $\{f_{Lx}, f_{Ly}, f_{Rx}, f_{Ry}\}$ are unknown.

Since the coordinates of the ends of the rope are now known as function of time, we need n generalized coordinates, $\{\theta_1, \theta_2, \cdots, \theta_n\}$. Equations (10)-(14) and the expression for the kinetic energy, (16), still remain the same. However now we have just n generalized forces,

$$\begin{aligned} Q_{\theta_i} &= -f_{Rx} L_i \sin(\theta_i) + f_{Ry} L_i \cos(\theta_i) \\ &\quad + \tau_i + \sum_{j=1}^{n} \mathbf{F}_j \cdot \frac{\partial \mathbf{p}_j}{\partial \theta_i} \qquad \forall\, i = 1, 2, \cdots, n \end{aligned} \tag{18}$$

Thus, now we have n Lagrange equations of motion,

$$\frac{d}{dt}\left(\frac{\partial K}{\partial \dot{\theta}_i}\right) - \frac{\partial K}{\partial \theta_i} - Q_{\theta_i} = 0 \tag{19}$$

Taking the time derivative of Equation (12) we obtain the velocity constraint equations,

$$\begin{bmatrix} \dot{x}_R \\ \dot{y}_R \end{bmatrix} - \begin{bmatrix} \dot{x}_L \\ \dot{y}_L \end{bmatrix} - \sum_{j=1}^{n} L_j \dot{\theta}_j \begin{bmatrix} -\sin(\theta_j) \\ \cos(\theta_j) \end{bmatrix} = 0 \tag{20}$$

And differenciating it for a second time we obtain the acceleration constraint,

$$\begin{bmatrix} \ddot{x}_R \\ \ddot{y}_R \end{bmatrix} - \begin{bmatrix} \ddot{x}_L \\ \ddot{y}_L \end{bmatrix} - \sum_{j=1}^{n} L_j \left(\ddot{\theta}_j \begin{bmatrix} -\sin(\theta_j) \\ \cos(\theta_j) \end{bmatrix} - \dot{\theta}_j^2 \begin{bmatrix} \cos(\theta_j) \\ \sin(\theta_j) \end{bmatrix} \right) = 0 \tag{21}$$

Equations (19) and (21) together form $n+2$ equations, which are algebraic in the unknowns f_{R_x} and f_{R_y}, whereas second order ordinary differential equations in the unknowns $\theta_1, \theta_2, \cdots, \theta_n$. Moreover they are affine in $\{f_{R_x}, f_{R_y}, \ddot{\theta}_1, \ddot{\theta}_2, \cdots, \ddot{\theta}_n\}$. Thus, for given trajectories of the left and right ends of the rope (*i.e.* given $\{x_L, y_L, x_R, y_R\}$ and their derivatives as a function of time), and an initial configuration $\{\theta_1, \theta_2, \cdots, \theta_n\}$ that satisfy the shape constraint equations (12), and an initial set of angular speeds $\{\dot{\theta}_1, \dot{\theta}_2, \cdots, \dot{\theta}_n\}$ that satisfy the velocity constraint equations (20) at $t = 0$, we can integrate and solve Equations (19) and (21) for $\{f_{R_x}, f_{R_y}, \theta_1, \theta_2, \cdots, \theta_n\}$.

As in the force controlled case, for simulating the system we used Mathematica for simplifying the Equations (19) and (21) to obtain the algebraic-differential equations, and the coefficients of the unknown quantities in the equations. The equations were then solved and numerically integrated using C and Matlab. The accompanying video shows the simulation results. Figure 5(e)-5(h) shows an example run of the position controlled system simulation.

IV. The Quasi-static model

In this section we simplify the discrete segment model in order to implement a method for controlling the shape of the linkage. The quasi-static model for position control is obtained by setting the inertial forces equal to zero. This assumption is reasonable when drag forces dominate over inertial forces and is justified for slow-moving boats, as we will see Section V. Under this condition, the equations that govern the evolution of the system simplify to

$$Q_{\theta_i} = 0, \quad \forall\, i = 1, 2, \cdots, n \tag{22}$$

where Q_{θ_i} are given by Equations (18). Along with the velocity constraint equations (20), these make a total of $n+2$ equations.

We now make certain interesting observations about these equations. First we note that each of the external forces, $\mathbf{F}_j$, and torques, τ_j, due to drag are linear in the speeds $\{\dot{x}_L, \dot{y}_L, \dot{x}_R, \dot{y}_R, \dot{\theta}_1, \dot{\theta}_2, \cdots, \dot{\theta}_n\}$. Thus from (18), Q_{θ_i} are linear in the variables $\{\dot{x}_L, \dot{y}_L, \dot{x}_R, \dot{y}_R, \dot{\theta}_1, \dot{\theta}_2, \cdots, \dot{\theta}_n, f_{Rx}, f_{Ry}\}$. Moreover the velocity constraint equations (20) are linear in $\{\dot{x}_L, \dot{y}_L, \dot{x}_R, \dot{y}_R, \dot{\theta}_1, \dot{\theta}_2, \cdots, \dot{\theta}_n\}$. Thus, the $n+2$ equations, (22) and (20), are linear in $n+6$ variables, $\{\dot{x}_L, \dot{y}_L, \dot{x}_R, \dot{y}_R, \dot{\theta}_1, \dot{\theta}_2, \cdots, \dot{\theta}_n, f_{Rx}, f_{Ry}\}$.

One can eliminate f_{Rx} and f_{Ry} from these equations. This leaves n equations which are linear in $n+4$ quantities, $\{\dot{x}_L, \dot{y}_L, \dot{x}_R, \dot{y}_R, \dot{\theta}_1, \dot{\theta}_2, \cdots, \dot{\theta}_n\}$. These equations that govern the evolution of the quasi-static model, can be written as

$$A_{n\times 4}\dot{P} + B_{n\times n}\dot{\Theta} = 0 \tag{23}$$

where, $\dot{P} = [\dot{x_L}, \dot{y_L}, \dot{x_R}, \dot{y_R}]^T$ and $\dot{\Theta} = [\dot{\theta_1}, \dot{\theta_2}, \cdots, \dot{\theta_n}]^T$.

Note that the matrices $A_{n\times 4}$ and $B_{n\times n}$ contain only the shape variables $x_L, y_L, x_R, y_R, \theta_1, \theta_2, \cdots, \theta_n$. For a given shape and the control speeds $\dot{P} = \{\dot{x_L}, \dot{y_L}, \dot{x_R}, \dot{y_R}\}$ applied to the ends of the linkage, the angular speeds of the segments, and hence the evolution of the shape, is given by

$$\dot{\Theta} = -B^{-1}A\dot{P} \tag{24}$$

Equation (24) describes the dynamics of the quasi-static model.

V. Field Experiments

To ground the models developed in the previous sections, we performed data-collections trials in the field. Field data were recorded in Echo Park Lake, Los Angeles using two ASVs designed by the University of Southern Californias Robotic Embedded Systems Lab (RESL). Each ASV is an OceanScience QBoat-I hull with a length of 2.1 m and a width of 0.7 m at the widest section. Each boat weighs 48 kg with instrumentation and batteries. The onboard computing package consists of a Mini-ITX 2 GHz dual-core computer. A 28 Ah sealed lead acid (SLA) battery is used to power the computer and all sensors, and a 32 Ah AGM battery is used for the drive motors and the rudder. The vehicles have a nominal runtime of 6 hours.

The vehicle sensor suite used in the experiments reported here is a navigation package. Both vehicles are equipped with a uBlox EKF-5H GPS that provides global position updates at 2 Hz, and a Microstrain 3D-M IMU with integrated compass sampled at 50 Hz. The ASVs are controlled by software built using the open-source framework Robot Operating System (ROS) [8]. ROS provides a structured communications layer on top of the operating system, allowing intercommunicating nodes and services to be developed easily.

Each data recording run in the field proceeded as follows. Both ASVs were manually driven at linear speed v and an initial separation distance D between them. Traces from the following combinations of D and v were recorded.

$D(m)$	$v(m/s)$
4	0.8, 1.0, 1.4
6	0.6, 0.9, 1.2
8	0.6, 0.7, 0.8, 0.9, 1.0
10	0.5, 0.7, 0.8
12	0.5, 0.75

For each combination, the ASVs were driven manually at the chosen speeds with the initial separation distance D. A 60 ft hollow diamond-braided polypropylene rope with $3/4$ in diameter was attached to each ASV (one vehicle at either end of the rope). The rope was chosen so it would float on the water surface. Markers were placed evenly along the rope for improved visibility and to help with verification of the data processing. Figure 6 shows a snapshot of one of the trials in progress.

For detecting the rope, each boat was equipped with a single Microsoft LifeCam Cinema USB video camera looking backwards towards the dragged rope on the water surface. To obtain the rope shape from the video images, the rope pixel coordinates were manually extracted from selected frames. Since the rope lies in a plane, a perspective transform [6] maps the image plane to the real world plane. The transform was calculated for each ASV using a set of measured point correspondences. Since the data were gathered in a relatively still lake at a low speed, the roll and pitch of the ASVs was minimal. Changes in roll and pitch were ignored in the estimation of the shape of the rope.

Fig. 6. A snapshot of one of the data-gathering trials. The two ASVs and the rope are visible. The markers had not been placed on the rope in this trial.

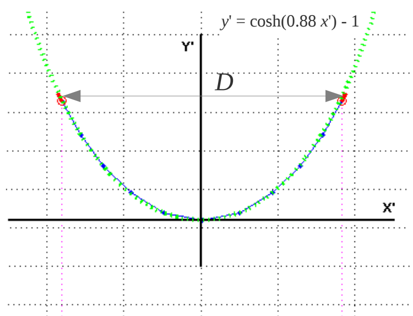

(a) A catenary curve (green dotted) overlayed on the complete dynamic simulated steady-state shape of the rope (blue) pulled by two boats (red) along a *straight line*.

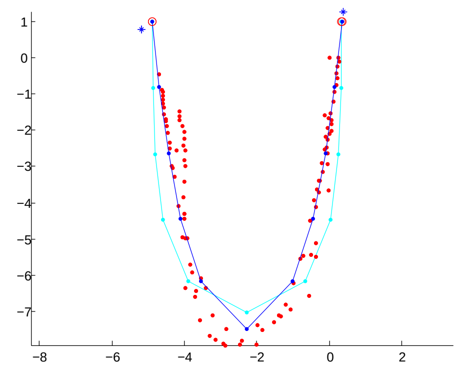

(b) Steady-state shapes from simulation overlayed on experimental rope data. The cyan configuration is for $c_S = 0.05, c_V = 0.0$. The blue configuration represents $c_S = c_V = 0.05$.

Fig. 7.

The cameras took snapshots of the shape of the rope when the boats were moving parallel to each other in a straight line and the rope was in a steady state. The perspective transform, $\mathbf{X} = H\mathbf{x}$, used to transform a point from pixel coordinates, $\mathbf{x} = (x, y, 1)^T$, to a point in metric coordinates relative to the ASVs, $\mathbf{X} = (X, Y, W)$, was determined using the non-homogeneous linear solution [3]. The transform was applied to the manually extracted rope pixels along the rope to transform them to a coordinate system relative to each ASV. Using the position of each boat from GPS, the orientation from the IMU, the rope coordinates for both ASVs were transformed to the same coordinate system for further processing.

Knowing the speeds of the boat and the separation D between the boats at steady state, we compare the experimental shape of the rope with the steady-state shape predicted by the discrete segment quasi-static model described earlier. Figure 7(b) shows one such frame, where the red dots represents points on the rope, and the model predictions are overlayed on it. The configuration shown in light cyan is the case where $c_S = 0.05, c_V = 0.0$, whereas the darker blue configuration is the case where $c_S = c_V = 0.05$. Clearly, $c_S = c_V = 0.05$ matches the experimental data, thus substantiating the catenary analogy described in Section II-C.

VI. Applications to Rope Shape Control and Coverage Maximization

We now have a quasi-static discrete model for the rope, and realistic values of the drag coefficients for the experimental ASVs (from field trials). We now apply the model to two problems.

A. Shape Control

In the first problem, a desired shape of the rope is specified and a control law is designed to drive the discrete quasi-static model described in Section IV to the specified shape.

Denote the desired shape of the discrete model by $\Theta^D = [\theta_1^D, \theta_2^D, \cdots, \theta_n^D]^T$. We want to design the control speeds of the two rope ends, $\dot{x}_L, \dot{y}_L, \dot{x}_R, \dot{y}_R$, so as to achieve $\theta_i = \theta_i^D,\ i = 1, \cdots, n$. We propose the control law

$$\dot{P} = -A^+ BK(\Theta^D - \Theta) \tag{25}$$

where, $(\cdot)^+$ is the Moore-Penrose pseudoinverse, and K is an $n \times n$ gain matrix.

For $n > 4$ this control law is definitely not guaranteed to achieve the desired shape exactly, since we do not have full controllability of the system. Figure 8 shows an attempt to control the shape of a 10-segment model with the gain matrix $K = 0.1I$, and the desired shape of $\Theta_D = [2.83, 2.20, 1.57, 0.94, 0.31, -0.31, -0.94, -1.57, -2.20, -2.83]^T$ (in radians) that

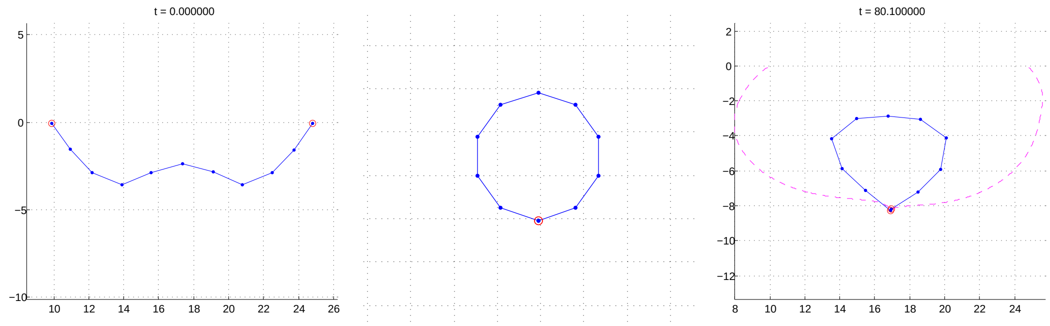

(a) Initial shape. (b) Desired shape. (c) Final shape attained.

Fig. 8. Shape control example: Desired shape is an approximate circle. The dashed magenta curves in (c) show the trajectories followed by the boats.

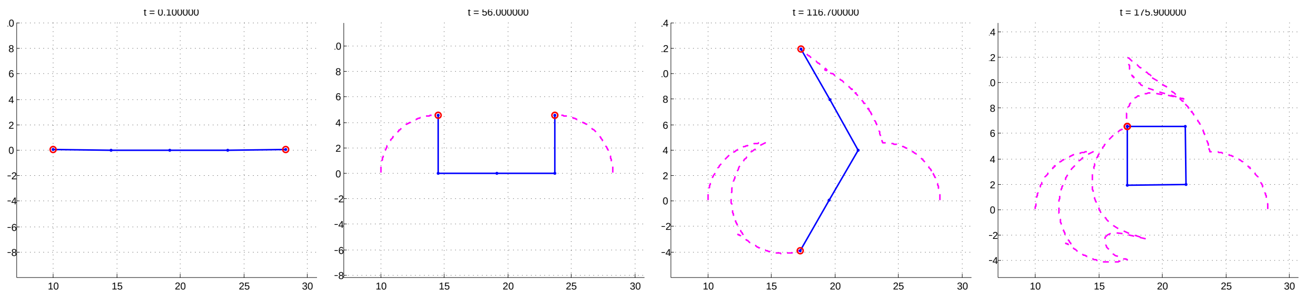

(a) Initial shape. (b) U-shape. (c) A right-pointed V. (d) Enclosure in a box.

Fig. 9. Shape control with complete controllability for a 4-link model. Starting from a straight line configuration, we consecutively change ths shape to the form of an "U", followed by that of a right-pointed "V", and finally to a square enclosure. The dashed magenta curves show the trajectories followed by the boats.

approximates a circle with the boats places at the south end of it (Figure 8(b)). As evident from Figure 8(c), the controller was able to achieve a satisfactory approximation of the desired shape.

However we note that when $n = 4$, the inverse of A exists, and hence we have full controllability of the system. From Equation (24) and (25) the system dynamics becomes $\dot{\Theta} = K(\Theta^D - \Theta)$. Thus, for any K with positive eigenvalues, Θ is guaranteed to converge to Θ^D. Figure 9 illustrates such a system made up of 4 links. Starting from a straight line configuration, we consecutively attain the exact desired shape of an "U" (Figure 9(b)), followed by that of a right-pointed "V" (Figure 9(c)), and finally a square enclosure (Figure 9(d)). The gain matrix used is $K = 0.1I$.

B. *Coverage Maximization*

The second application is to maximize the coverage area swept by the rope given a contraint on the maximum ASV speeds. For this, consider a steady-state (and quasi-static) motion of the ASVs parallel to each other in a straight line (Figure 7(a)). Starting from an arbitrary initial configuration, and letting $\dot{x}_L = 0, \dot{y}_L = v_0, \dot{x}_R = 0, \dot{y}_R = v_0$, we can numerically obtain the steady state configurations and drags by letting the system evolve according to (24) until steady-state is achieved. The force that each boat needs to exert at the steady state, $f_{L_x}, f_{L_y}, f_{R_x}, f_{R_y}$ can then be computed from the quasi-static model (Equations 22) or directly from the force equations. Due to symmetry, the force applied by each boat is $f_0 = \sqrt{f_{Lx}^2 + f_{Ly}^2} = \sqrt{f_{Rx}^2 + f_{Ry}^2}$. At steady state, this force, f_0, depends on the separation D between the boats. Figure 10(a) shows this dependence (numerically evaluated) when the speed $v_0 = 1.0$. In the plot, both the values of f_0 and D have been normalized by total length of the linkage, L.

As noted in the previous section, from the experimental results, the practical scenario is the case when $c_S = c_V = 0.05$. Thus in the following discussion we concentrate on the $c_S = c_V = 0.05$ case. So far we have obtained the functional form g such that $f_0/L = g(D/L)$ at $v_0 = 1.0$. We also note that f_0 should be linear in v_0 since in the steady state the only external forces that the ASVs overcome are the drag forces, which are linear in the speeds. Thus we conclude $f_0/L = v_0 \; g(D/L)$. Thus, if we know that the maximum force that an ASV can exert is f_{max}, the maximum attainable speed and the separation between the boats will be related by $f_{max}/L = v_{max} \; g(D/L)$. The rate at which area is swept by the rope is thus given by

$$\Phi = v_{max} \; D = (f_{max}/L)\frac{D}{g(D/L)} = f_{max}\frac{D/L}{g(D/L)} \tag{26}$$

A plot of Φ against normalized separation (*i.e.* D/L) for $f_{max} = 1.0$ is shown in Figure 10(b). The maximum rate of area sweep is attained when the inter-vehicle separation D is close to 0.8 times the length of the rope.

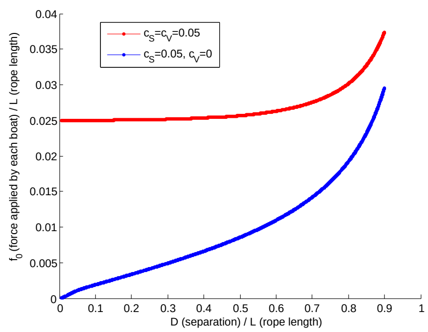

(a) f_0/L plotted against the normalized separation between the boats, D/L. The upper curve is for the case $c_S = c_V = 0.05$, and the lower curve is for $c_S = 0.05, c_V = 0.0$.

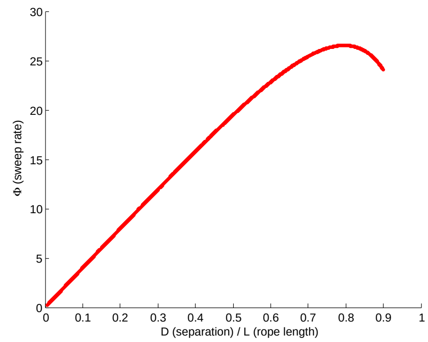

(b) Area sweep rate, Φ, plotted against the normalized separation between the boats, D/L, when $f_{max} = 1.0$.

Fig. 10.

VII. Conclusions

In this paper we have derived from first principles the PDEs that govern the dynamics of a flexible rope being pulled by two Autonomous Surface Vehicles on the water surface. We have also proposed a discrete model and derived a numerical solution for it. We have experimentally validated the model under certain special cases. We proposed a control law for controlling the shape of the discrete model under quasi-static assumptions. We studied the relationship between the rate of swept area coverage, the maximum force that each vehicle can apply, the separation between the vehicles and their speed. We derive the condition under which the coverage rate is maximized - an important capability for efficient skimming operations. In the future we plan to extend this work to incorporate complex planning problems and strategies for capturing oil patches on the water surfaces via caging. We also plan to perform novel shape control using more than two ASVs.

VIII. Acknowledgements

We gratefully acknowledge support from the ONR Antidote MURI project, grant no. N00014-09-1-1031. SB and VK acknowledge support from ONR Grant N00014-08-1-0696 and NSF Grant IIP-0742304. HH and GS were supported in part by the NOAA MERHAB program (NA05NOS4781228), NSF as part of the Center for Embedded Network Sensing (CENS) (CCR-0120778) and the ONR SoA program.

References

[1] F. Arrichiello, H. Heidarson, S. Chiaverini, and G. Sukhatme. Cooperative caging and transport using autonomous aquatic surface vehicles. *Submitted to IEEE Transactions on Robotics*, 2010.

[2] M.Y.H. Bangash and T.Bangash. *Elements of spatial structures: analysis and design*. Thomas Telford, Ltd., 2003.

[3] A. Criminisi, I. Reid, and A. Zisserman. A plane measuring device. *Image and Vision Computing*, 17(8):625–634, 1999.

[4] Robert W. Fox, Alan T. McDonald, and Philip J. Pritchard. *Introduction to Fluid Mechanics*. Wiley, 2005.

[5] Herbert Goldstein, Charles P. Poole, and John L. Safko. *Classical Mechanics*. Addison Wesley, 2001.

[6] R. Hartley and A. Zisserman. *Multiple View Geometry in Computer Vision*. Cambridge University Press, 2003.

[7] Richard A. Kerr. A lot of oil on the loose, not so much to be found. *Science*, 329(734), 2010.

[8] M. Quigley, B. Gerkey, K. Conley, J. Faust, T. Foote, J. Leibs, E. Berger, R. Wheeler, and A. Ng. Ros: An open-source robot operating system. In *Proceedings of the Open-source software workshop at ICRA 2009*. 2009.

[9] Campbell Robertson and Clifford Krauss. Gulf spill is the largest of its kind, scientists say. *The New York Times*, August 2010.

[10] D. J. Tritton. *Physical Fluid Dynamics (Oxford Science Publications)*. Oxford University Press, USA, 1988.